



ALMA MATER STUDIORUM
UNIVERSITÀ DI BOLOGNA

ARCHIVIO ISTITUZIONALE
DELLA RICERCA

Alma Mater Studiorum Università di Bologna Archivio istituzionale della ricerca

Measurement of Jupiter's asymmetric gravity field

This is the final peer-reviewed author's accepted manuscript (postprint) of the following publication:

Published Version:

Measurement of Jupiter's asymmetric gravity field / Iess, L.*; Folkner, W.M.; Durante, D.; Parisi, M.; Kaspi, Y.; Galanti, E.; Guillot, T.; Hubbard, W.B.; Stevenson, D.J.; Anderson, J.D.; Buccino, D.R.; Casajus, L. Gomez; Milani, A.; Park, R.; Racioppa, P.; Serra, D.; Tortora, P.; Zannoni, M.; Cao, H.; Helled, R.; Lunine, J.I.; Miguel, Y.; Militzer, B.; Wahl, S.; Connerney, J.E.P.; Levin, S.M.; Bolton, S.J.. - In: NATURE. - ISSN 0028-0836. - STAMPA. - 555:7695(2018), pp. 220-222. [10.1038/nature25776]

Availability:

This version is available at: <https://hdl.handle.net/11585/632494> since: 2018-03-28

Published:

DOI: <http://doi.org/10.1038/nature25776>

Terms of use:

Some rights reserved. The terms and conditions for the reuse of this version of the manuscript are specified in the publishing policy. For all terms of use and more information see the publisher's website.

This item was downloaded from IRIS Università di Bologna (<https://cris.unibo.it/>).
When citing, please refer to the published version.

(Article begins on next page)

This is the final peer-reviewed accepted manuscript of:

*less, L., Folkner, W., Durante, D. et al. **Measurement of Jupiter's asymmetric gravity field**. Nature 555, 220–222 (2018)*

The final published version is available online at:

<https://doi.org/10.1038/nature25776>

Rights / License:

The terms and conditions for the reuse of this version of the manuscript are specified in the publishing policy. For all terms of use and more information see the publisher's website.

This item was downloaded from IRIS Università di Bologna (<https://cris.unibo.it/>)

When citing, please refer to the published version.

1 **The measurement of Jupiter's asymmetric gravity field**

2 L. Iess^{1*}, W.M. Folkner², D. Durante¹, M. Parisi², Y. Kaspi³, E. Galanti³, T. Guillot⁴, W.
3 B. Hubbard⁵, D.J. Stevenson⁶, J.D. Anderson⁷, D. R. Buccino², L. Gomez Casajus⁸, A.
4 Milani⁹, R. Park², P. Racioppa¹, D. Serra⁹, P. Tortora⁸, M. Zannoni⁸, H. Cao⁶, R.
5 Helled¹⁰, J.I. Lunine¹¹, Y. Miguel⁴, B. Militzer¹², S. Wahl¹², J.E.P. Connerney¹³, S.M.
6 Levin², S.J. Bolton⁷

7 ¹*Sapienza Università di Roma, 00184 Rome, Italy*

8 ²*Jet Propulsion Laboratory/Caltech, Pasadena, CA 91109, USA*

9 ³*Weizmann Institute of Science, Rehovot 76100, Israel*

10 ⁴*Observatoire de la Côte d'Azur, 06304 Nice, France.*

11 ⁵*Lunar and Planetary Laboratory, University of Arizona, Tucson, AZ 85721, USA*

12 ⁶*California Institute of Technology, Pasadena, CA 91125, USA.*

13 ⁷*Southwest Research Institute, San Antonio, TX 78238, USA*

14 ⁸*Università di Bologna, 47100 Forlì, Italy*

15 ⁹*Università di Pisa, 56127 Pisa, Italy*

16 ¹⁰*University of Zurich, 8057 Zurich, Switzerland*

17 ¹¹*Cornell University, Ithaca, NY 14853, USA*

18 ¹²*University of California, Berkeley, CA 94720, USA*

19 ¹³*NASA Goddard Space Flight Center, Greenbelt, MD 20771, USA*

20 ***Corresponding author. Email: luciano.iess@uniroma1.it**

21

22 **The gravity harmonics of an oblate rotating planet can be decomposed into static**
 23 **components (arising from solid body rotation) and dynamic components. Within**
 24 **the framework of models of the gas giant planets, even zonal components J_{2n} are**
 25 **approximately proportional to q^n , where q is the ratio between centrifugal**
 26 **acceleration and gravity at the equator¹. Any asymmetry in the gravity field is**
 27 **attributed to differential rotation and deep atmospheric flows. The odd harmonics,**
 28 **J_3, J_5, J_7, J_9 and higher, are a measure of the depth of the winds in the different**
 29 **zones of the atmosphere^{2,3}. Here we report measurements of Jupiter's gravity**
 30 **harmonics (both even and odd) through precise Doppler tracking of the Juno**
 31 **spacecraft in its polar orbit around Jupiter. We find a north-south asymmetry,**
 32 **which is the signature of atmospheric and interior flows. The analysis of the**
 33 **harmonics is done in two companion papers^{4,5}.**

34 The external, harmonic, gravitational potential of a body can be expanded in a series of
 35 complex spherical harmonic functions $Y_{lm}(\theta, \varphi)$ (an orthonormal basis for functions
 36 defined on the unit sphere) multiplied by a scaling factor depending on a normalized
 37 radial distance r/R

$$U(r, \theta, \varphi) = -\frac{GM}{r} \left[1 + \sum_{l \geq 2} \left(\frac{R}{r}\right)^{l+1} \sum_{m=-l}^l U_{lm} Y_{lm}(\theta, \varphi) \right]$$

38 For a planet, R is generally chosen as the equatorial radius of the body. Were the
 39 internal density ρ of the body known, the harmonic coefficients U_{lm} could be obtained
 40 from the integral over the volume V of the body⁶

$$U_{lm} = \frac{1}{(2l+1)MR^l} \int_V r'^l Y_{lm}(\theta', \varphi') \rho(r', \theta', \varphi') dV'$$

41 When the density does not depend on longitude, as expected for a fluid and rapidly
 42 rotating planet like Jupiter, the above expression simplifies in

$$J_l \equiv -U_{l0} = -\frac{1}{(2l+1)MR^l} \int_V r'^l P_l(\theta') \rho(r', \theta') dV'$$

43 where P_l is the Legendre polynomial of degree l . Thus, zonal coefficients J_l bear
 44 important, although non-unique, information on the density distribution inside Jupiter.

45 On July 4, 2016 the Juno spacecraft was captured by the gravity field of Jupiter,
 46 starting its prime mission devoted to the investigation of the deep interior, the
 47 magnetosphere, and the atmosphere of the planet. The spacecraft is currently in a highly
 48 eccentric ($e=0.98$), long period (52.9 days), polar orbit, with a pericenter altitude of
 49 about 4000 km above the 1 bar level as inferred from radio occultations⁷.

50 As a consequence of the equivalence principle, gravity field determinations
 51 require the measurement of the relative motion between (at least) two masses. In the
 52 Juno gravity experiment, the spacecraft acts as a test particle falling in the gravity field
 53 of the planet. The Earth is the second end mass. Jupiter's gravity is inferred from range
 54 rate measurements between a ground antenna and the spacecraft during pericenter
 55 passes. In Juno gravity determinations, the ground station transmits two carriers,
 56 respectively at 7,153 MHz (X-band) and 34,315 MHz (Ka band). Onboard, a X band
 57 transponder and a dedicated Ka band frequency translator (a radio science instrument)
 58 lock the incoming carriers and retransmit them back to ground at 8,404 MHz and 32,088
 59 MHz. The range rate (Doppler) observable is obtained by comparing the transmitted and
 60 received frequencies. Juno is the first deep space mission using Ka band radio systems
 61 for planetary geodesy. Ka band and multifrequency radio links were previously
 62 employed only for precision tests of relativistic gravity with the Cassini spacecraft in
 63 the cruise phase^{8,9}. Due to the dispersion properties of plasmas, Ka band radio links

64 provide excellent immunity to the adverse effects of charged particles along the
65 propagation path, including the Io torus (a potential source of bias in the gravity
66 estimates¹⁰). The Juno radio system enables a further reduction of plasma noise
67 (approximately 75%) by combining X and Ka band Doppler observables¹¹. In order to
68 reduce the noise from tropospheric water vapour, a radiometer placed near the ground
69 antenna was continuously monitoring the wet path delay along the line of sight.

70 Our analysis is based on the first two Ka band gravity passes of Juno, labelled PJ3
71 (11 December 2016) and PJ6 (19 May 2017). Doppler measurements were integrated
72 over 60 s prior to processing in order to enable adequate sampling of the gravity signal.
73 At this time scale the measured two-way range rate noise at Ka band was 2×10^{-5} m/s at
74 60 s, in line with the expectations from Ka band radio link noise models¹². The Doppler
75 noise is approximately white between 4×10^{-4} and 2×10^{-2} Hz (the characteristic
76 frequency range of the gravity signal).

77 The dynamical model used in the orbital fit is driven by the theoretical
78 expectations for the gravity field of gaseous planets. We adopt here the standard
79 spherical harmonics representation of planetary gravity fields, whose expansion
80 coefficients are determined by the density distribution inside the body⁶. Models of the
81 interior structure predict that Jupiter's gravity is dominated by an axially and
82 hemispherically symmetric component due to solid body rotation^{13,14}. This component
83 is determined by the radial density distribution in the rotating planet and is represented
84 by even zonal harmonic coefficients $J_{2n} \sim q^n$. Atmospheric and internal dynamics can
85 produce small density perturbations that result in a more complex gravity
86 representation, involving odd zonal and possibly tesseral harmonics, as well as small
87 corrections to the even zonal harmonics^{3,5,15}. The latter are however indiscernible from
88 the much larger contribution of solid body rotation up to harmonics of degree 12, where
89 the dynamics is expected to lead the gravity signal². Hence, any detection of an

90 asymmetric (hemispherically or axially) gravity field would be a unique indication of
91 internal dynamics due to flows. Juno tracking data have provided the first ever evidence
92 of hemispherical (North-South) asymmetries in the gravity field of a giant planet.

93 Prior to PJ3, the best determination of Jupiter's even zonal gravity field was
94 carried out using lower quality Doppler observables from the first two Juno pericenter
95 passes (PJ1 and PJ2)^{16,17}. These early results improved previous determinations of the
96 zonal harmonic coefficients J_4 and J_6 ^{18,19} and allowed the first determination of J_8 .
97 Those measurements of J_4 and J_6 have been used to constrain the radial density profile
98 of the planet²⁰. However, the magnitude of the much smaller odd zonal field could not
99 be determined, because of the unfavourable observation geometry and the large
100 propagation noise caused by the interplanetary plasma on the X band uplink (7.2 GHz).

101 High accuracy Ka band data acquired during PJ3 and PJ6 provided the first
102 determination of the asymmetric component of Jupiter's gravity (Fig. 1 and Table 1).
103 We processed Doppler data using orbit determination codes developed for spacecraft
104 navigation (JPL software MONTE) and an external estimation filter. Data from PJ3 and
105 PJ6 were separately fitted for the spacecraft state vector at the beginning of the tracking
106 pass (about 6 h prior to transit at pericenter), Jupiter's gravitational parameter GM , the
107 zonal harmonic coefficients J_2 - J_{24} , the tesseral quadrupole harmonics, the pole position
108 and rate at epoch J2017.0, and the k_{22} Love number. This set of parameters allows
109 fitting all data to the noise level. The $l=2$ tesseral coefficients, although not strictly
110 required by a least size solution, have been estimated to search for a possible deviation
111 of the principal axis of inertia from the spin axis. The masses and the ephemerides of
112 the Jovian satellites are adopted from JUP 310¹⁹ and not estimated, although their
113 uncertainties have been considered in the final covariance matrix. A linear correction to
114 the orbit of Jupiter was applied in order to fit range data acquired at X band during the
115 tracking pass. The relativistic Lense-Thirring precession is included, and the magnitude

116 of Jupiter's polar moment of inertia set to interior model predictions, considered with a
 117 20% of uncertainty (affecting the recovery of Jupiter's spin axis). The single-arc
 118 solutions were then combined in a global multi-arc solution made up by two categories
 119 of parameters: local (pertaining to each arc) and global (common to both arcs). Only
 120 spacecraft initial conditions are treated as local parameters. No constraints have been
 121 applied to the global parameters except Jupiter's GM , whose current estimate is more
 122 accurate than that obtained so far from Juno¹⁰. The data are weighted according to the
 123 Doppler noise in each Ka band pass, assuming no correlation between samples. The
 124 correctness of this assumption is verified a posteriori from the nearly white power
 125 spectral density of the residuals in the frequency band of interest¹⁰.

126 The two single-arc gravity solutions are fully compatible at 2σ except J_4 (3.5σ ;
 127 see Fig. 2 for some examples). Fitting jointly PJ3 and PJ6 data does not require any
 128 tesseral component other than the quadrupole, even if the two ground tracks are
 129 separated by about 150° . However, available data do not allow setting a reliable upper
 130 limit to tesseral harmonics, although numerical simulations indicate that a tesseral field
 131 corresponding to a flow depth larger than 380 km would produce signatures in the
 132 Doppler residuals^{10,21}. Consider covariances corresponding to this flow depth are larger
 133 than the uncertainties reported in Table 1¹⁰. The current data set does not show evidence
 134 of a time-varying gravity field, as may result from Jupiter's normal modes²².

135 Since for large-scale flows on rotating planets wind shear is accompanied by
 136 density gradients, it is possible to directly link the flows and the gravity field. The
 137 velocity gradient affects both the even and odd zonal harmonic coefficients, but only the
 138 odd coefficients bear the unique signature of the dynamics when $l < 10$ (for $l > 10$ also the
 139 even coefficients are dominated by the dynamics of the flows - see Fig. 1). We singled
 140 out the contribution of the winds by removing the J_2, J_4, J_6, J_8 harmonic components
 141 from the complete gravity potential. The North-South asymmetric component of the

142 gravity acceleration reaches the largest magnitude of 3.4 ± 0.4 mGal (3σ) at a latitude of
 143 24°N , approximately at the transition between the Northern Equatorial Belt and the
 144 Northern Tropical Zone (Fig. 3). Remarkably, this region corresponds to a large
 145 velocity and latitudinal gradient of surface winds, as expected for a gravity signal due to
 146 wind dynamics^{4,15}. The odd zonal harmonics J_3, J_5, J_7, J_9 and the associated gravity
 147 acceleration may be used to infer the depth and the vertical profile of the winds^{3,4}.

148 References

- 149 1. Lanzano, P. The equilibrium of a rotating body of arbitrary density. *Astrophys.*
 150 *Space Sci.* 29, 161-178 (1974).
- 151 2. Hubbard, W. B. Note: Gravitational signature of Jupiter's deep zonal flows.
 152 *Icarus* 137, 357–359 (1999).
- 153 3. Kaspi, Y. Inferring the depth of the zonal jets on Jupiter and Saturn from odd
 154 gravity harmonics. *Geophys. Res. Lett.* **40**, 676–680 (2013).
- 155 4. Kaspi, Y., et al. Jupiter's deep atmosphere revealed by Juno's asymmetric
 156 gravity measurements, *Nature* (2018), this issue.
- 157 5. Guillot, T., et al. Suppressed differential rotation in Jupiter's deep interior,
 158 *Nature* (2018), this issue.
- 159 6. Bertotti, B., Farinella, P., & Vokrouhlicky, D. (2012). Physics of the solar
 160 system: dynamics and evolution, space physics, and spacetime structure, p. 45,
 161 Springer (2012), with earlier references therein.
- 162 7. Lindal, G. F., et al. The atmosphere of Jupiter: An analysis of the Voyager radio
 163 occultation measurements. *J. Geophys. Res.* **86**, 8721-8727 (1981).
- 164 8. Bertotti, B., L. Iess, and P. Tortora A test of general relativity using radio links
 165 with the Cassini spacecraft. *Nature* **425**, 374-376 (2003).

- 166 9. Armstrong, J.W., Iess, L., Tortora, P. & Bertotti, B. Stochastic gravitational
167 wave background: upper limits in the 10-6-10-3 Hz band. *Astrophys. J.*, **599**,
168 806-813 (2003).
- 169 10. See Methods section.
- 170 11. Bertotti, B., Comoretto, G. & Iess, L. Doppler tracking of spacecraft with
171 multifrequency links. *Astron. Astrophys.* **269**, 608-616 (1993).
- 172 12. Asmar, S. W., Armstrong, J. W., Iess, L. & Tortora, P. Spacecraft Doppler
173 tracking: Noise budget and accuracy achievable in precision radio science
174 observations. *Radio Science* **40**(2) (2004).
- 175 13. Hubbard, W. B. Effects of differential rotation on the gravitational figures of
176 Jupiter and Saturn. *Icarus*, **52**, 509–515 (1982).
- 177 14. Hubbard, W. B. & Militzer, B. A preliminary Jupiter model. *Astrophys. J.*, **820**,
178 80-93 (2016).
- 179 15. Kaspi, Y., Hubbard, W. B., Showman, A. P. & Flierl, G. R. Gravitational
180 signature of Jupiter’s internal dynamics. *Geophys. Res. Lett.* **37**, L01204 (2010).
- 181 16. Bolton, S. J., et al. Jupiter’s interior and deep atmosphere: The initial pole-to-
182 pole passes with the Juno spacecraft. *Science* **356**(6340), 821-825 (2017).
- 183 17. Folkner, W. M., et al. Jupiter gravity field estimated from the first two Juno
184 orbits. *Geophysical Research Letters* **44** (2017) doi:10.1002/2017GL073140.
- 185 18. Jacobson, R., Haw, R., McElrath T. & Antreasian P. A comprehensive orbit
186 reconstruction for the Galileo prime mission. *Adv. Astronaut. Sci.*, **103**, 465–
187 486. (1999),
- 188 19. Jacobson, R. A. Jupiter satellite ephemeris file Jup310, NASA Navigation and
189 Ancillary Information Facility. (2009), [Available at
190 https://naif.jpl.nasa.gov/pub/naif/generic_kernels/spk/satellites/jup310.bsp]

- 191 20. Wahl, S. M. *et al.* Comparing Jupiter interior structure models to Juno gravity
192 measurements and the role of an expanded core. *Geophys. Res. Lett.* **44**, 4649–
193 4659 (2017).
- 194 21. Parisi, M., et al. Probing the depth of Jupiter’s Great Red Spot with the Juno
195 gravity experiment. *Icarus* **267**, 232-242 (2016).
- 196 22. Durante, D., Guillot, T. & Iess, L. The effect of Jupiter oscillations on Juno
197 gravity measurements. *Icarus* **282**, 174-182 (2017).
- 198

199 **Acknowledgments**

200 The research described in this paper was carried out at the Sapienza University of
201 Rome, University of Bologna, and University of Pisa under the sponsorship of the
202 Italian Space Agency; at the Jet Propulsion Laboratory, California Institute of
203 Technology, under a contract with the NASA; by the Southwest Research Institute
204 under contract with the NASA. Support was provided also by the Israeli Space Agency
205 (YK and EG), and CNES (TG and YM). All authors acknowledge support from the
206 Juno Project. The data used in this paper will be available through the NASA Planetary
207 Data System.

208 **Author contributions**

209 L.I. and W.F. led the experiment and supervised the data analysis. L.I. wrote most of the
210 manuscript. D.D. and M.P. carried out the gravity data analysis. Y.K. and E.G. provided
211 models of the asymmetric and tesseral gravity field. Y.K., E.G., T.G., W.H., and D.J.S.
212 carried out consistency checks with interior models and provided theoretical support.
213 D.R.B. planned and supervised the data collection. P.R. designed and coded the orbit
214 determination filter used in this analysis. L.C., P.T., and M.Z. provided the media
215 calibrations. J.D.A., A.M., R.P., and D.S. advised in the data analysis. H.C., R.H., J.I.L.,

216 Y.M., B.M., and S.W. helped in the definition of the scientific objectives of the
 217 measurements. J.E.P.C., S.M.L., S.J.B. supervised the planning, execution, and
 218 definition of the gravity experiment.

219 **Author Information.** The authors declare that they have no competing financial
 220 interests. See npg.nature.com/reprintsandpermissions for reprints and permissions
 221 information. Correspondence and requests for materials should be addressed to L. Iess
 222 (email: luciano.iess@uniroma1.it).

223 **Table 1. Gravity solution**

	Value	Uncertainty
J_2 ($\times 10^6$)	14696.572	0.014
C_{21} ($\times 10^6$)	-0.013	0.015
S_{21} ($\times 10^6$)	-0.003	0.026
C_{22} ($\times 10^6$)	0.000	0.008
S_{22} ($\times 10^6$)	0.000	0.011
J_3 ($\times 10^6$)	-0.042	0.010
J_4 ($\times 10^6$)	-586.609	0.004
J_5 ($\times 10^6$)	-0.069	0.008
J_6 ($\times 10^6$)	34.198	0.009
J_7 ($\times 10^6$)	0.124	0.017
J_8 ($\times 10^6$)	-2.426	0.025
J_9 ($\times 10^6$)	-0.106	0.044
J_{10} ($\times 10^6$)	0.172	0.069
J_{11} ($\times 10^6$)	0.033	0.112
J_{12} ($\times 10^6$)	0.047	0.178
k_{22}	0.625	0.063
RA (deg)	268.0570	0.0013
Dec (deg)	64.4973	0.0014

225 **Legends**

226 **Table 1. Gravity solution.** Jupiter's gravity harmonics coefficients (un-normalised;
 227 reference radius = 71492 km), Love number k_{22} , pole coordinates at epoch J2017.0,
 228 obtained from PJ3 and PJ6 Juno science orbits. The deviation of the principal axis of
 229 inertia from the spin axis, as inferred from the uncertainty in C_{21} and S_{21} , is bound to be
 230 less than about 0.4 arcsec (130 m at the reference radius). J_2 includes a tidal term
 231 currently estimated at $\sim 2.98 \cdot 10^{-8}$. The associated uncertainties are realistic values to be
 232 used for analysis and interpretation. They correspond to three times the formal 1σ
 233 uncertainties.

234 **Fig. 1. Zonal gravity harmonic coefficients J_2 - J_{12} .** The dashed line shows the realistic
 235 uncertainty (Tab. 1). Positive and negative values are respectively in solid and empty
 236 circles.

237 **Fig. 2. 3σ uncertainty ellipses of J_3 - J_5 and J_7 - J_9 .** Brown and cyan ellipses refer
 238 respectively to single arc PJ3 and PJ6 solutions. The solid violet ellipse refers to the
 239 PJ3+PJ6 combined solution.

240 **Fig. 3. Gravity disturbances due to wind dynamics.** Latitudinal dependence of
 241 residual gravity acceleration (in mGal, positive outwards) and associated 3σ uncertainty
 242 (shaded area) at a reference distance of 71492 km, when gravity from even zonal
 243 harmonics J_2 , J_4 , J_6 and J_8 is removed. The residual gravity field, dominated by the
 244 dynamics of the flows, shows marked peaks correlated with the band structure. The
 245 latitudinal gradient of the measured wind profile is shown in the right panel. The largest
 246 (negative) peak of -3.4 ± 0.4 mGal (3σ) is found at a latitude of 24°N , where the
 247 latitudinal gradient of the wind speed reaches its largest value. The relation between the
 248 gravity disturbances and wind gradients is discussed in a companion paper⁴.

249

250 **Methods**

251 **Data acquisition.** Previous determinations of the Jovian gravity with Juno were carried
252 out by means of the standard radio system of the spacecraft at X band (7.2-8.4 GHz)
253 during the first two pericenter passes (PJ1 and PJ2). At these lower frequencies Doppler
254 data were marred by interplanetary plasma noise (although antenna mechanical noise
255 was an important noise source in PJ1). Our analysis is based on radio tracking of Juno
256 at Ka band during two pericenter transits on 11 December 2016 (17:03:40 UTC – PJ3)
257 and 19 May 2017 (06:00:45 UTC – PJ6). The use of Ka band provided an excellent
258 immunity to propagation noises due to charged particles. In the overall planning of the
259 mission, PJ3 and PJ6 were the first two pericenter passes devoted to gravity science.
260 Ground support was provided by DSS 25 (Goldstone, California), the only antenna of
261 NASA’s Deep Space Network (DSN) with two-way Ka band capabilities. Two-way Ka
262 and X band data were acquired from 12:47 UTC to 19:19 UTC during PJ3 (about 390
263 Doppler observables points at 60 s for each band), and from 01:39 UTC to 09:25 UTC
264 (about 460 Doppler observables per band) in PJ6. In order to improve the determination
265 of the spacecraft trajectory, we have used also data acquired in X band from an antenna
266 of the Canberra DSN complex (DSS 43) after the end of the DSS 25 pass, prior an orbit
267 trimming manoeuver.

268 Doppler data were obtained from a wide band open loop receiver used for radio science
269 investigations. A specially designed digital phase-locked loop has been applied to the 1
270 kHz complex samples of the received electric field to obtain the phase history and the
271 sky frequencies. Doppler data from the standard closed loop receiver are generally
272 noisier, thus resulting in larger formal uncertainties. Central values of the estimates
273 from the two data sets are statistically compatible.

274 **Non-gravitational accelerations.** The dynamical model used in the fit is purely
275 deterministic. All non-gravitational forces acting on the spacecraft are modelled by
276 means of a suitable set of parameters, whose uncertainties contribute to the final
277 covariance matrix. The largest non-gravitational acceleration is due to the solar
278 radiation pressure (about $9 \times 10^{-9} \text{ m/s}^2$) acting on the 61 m^2 solar panels and the 3 m high
279 gain antenna. Its modelling is simple, as the sun aspect angle, therefore also the
280 acceleration, is constant during the pass. We have assumed that the reflectivity of the
281 surfaces is known with a 20% uncertainty. Our dynamical model includes also the small
282 acceleration from the latitudinally varying, Jovian infrared emission ($1.2 \times 10^{-9} \text{ m/s}^2$ at
283 the equator) and the radiation pressure from the albedo of the planet ($6 \times 10^{-10} \text{ m/s}^2$). The
284 negligible effect on the gravity estimate due to inaccurate modelling on these non-
285 gravitational accelerations has been again assessed by means of numerical simulations.
286 The anisotropic thermal emission from the spacecraft and possible gas leaks may
287 produce small, additional, accelerations along the direction of the spin axis (the other
288 components being averaged out). As the direction of the Earth and the Sun differ by
289 only 9° during the observations, these accelerations are confused with the solar radiation
290 pressure and their effect in the estimate is accounted for in the 20% uncertainty
291 attributed to solar radiation pressure. Other accelerations, such as atmospheric and
292 magnetic drag, are too small to affect the gravity estimate.

293 **Orbit geometry.** The orbit geometry is a crucial factor in gravity determinations. The
294 key parameters are the orbital altitude and the angle between the line of sight and the
295 spacecraft acceleration. Juno's pericenter altitudes are sufficiently low (4154 km in PJ3
296 and 3503 km in PJ6) to reveal density inhomogeneities with spatial scales much smaller
297 than the radius of the planet. On the other hand, the large eccentricity causes the radial
298 distance from the planet to increase quickly with latitude, strongly reducing the
299 sensitivity to gravity disturbances in the polar regions (more markedly in the southern
300 hemisphere, due to the location of the pericenter north of the equator). The eccentricity

301 of the orbit limits also the gravitational contact time: the spacecraft covers 60 degrees in
302 latitude in about 1200 s, reaching a velocity of about 60 km/s at pericenter. The other
303 factor affecting the recovery of the gravity field is the orientation of the orbital plane
304 with respect to Earth, which controls the projection of the spacecraft velocity along the
305 line of sight. Although the angle between the opposite to the orbit normal and the Earth
306 direction is not optimal (19.2° in PJ3 and 15.1° in PJ6), the projected velocity and
307 acceleration still provide good observability of the zonal field.

308 The pericenter latitude undergoes secular variations due to Jupiter's oblateness,
309 allowing a more complete coverage of Jupiter's gravity. The pericenter drifts northward
310 by about 1° per orbit from an initial latitude of 2.7° . At the end of the nominal mission it
311 will reach a latitude of 32.6°N , allowing a better determination of gravity at high
312 northern latitudes. The node longitude is controlled by means of orbital manoeuvres to
313 target specific Jupiter longitudes and obtain a uniform coverage. These manoeuvres are
314 carried out far from pericenter and therefore do not affect the gravity determinations.
315 The orientation of the orbital plane with respect to Earth changes from a nearly face-on
316 configuration at orbit insertion to edge-on after about three years. Detailed information
317 on Juno's orbit can be obtained from NASA's HORIZONS system²³. Extended Data
318 Table 1 reports the main geometrical parameters relevant to gravity determination.

319 **Data quality and calibration.** We have carefully assessed and ruled out significant
320 biases in the gravity estimate due to systematic effects in the data and the dynamical
321 model. The largest systematic effect in Doppler measurement is due to the dry
322 troposphere, which causes path delay variations up to $\approx 3 \times 10^{-4}$ m/s over time scales of
323 6-8 hours. The suppression of this large signal is obtained using ground meteorological
324 data (mostly surface pressure and temperature) and a careful modelling of elevation-
325 dependent effects. Although a small residual tropospheric signal (mostly due to
326 horizontal pressure gradients) cannot be excluded, its time scale is much longer than

327 that from the gravity harmonics (10-30 minutes). Its effect on the gravity determination
328 is therefore negligible.

329 The path delay due to the ionospheric plasma is strongly reduced thanks to the use of
330 Ka-band. The Deep Space Network provides anyway calibrations of the ionospheric
331 path delays at each tracking complex by mapping dual frequency GPS measurements
332 onto the spacecraft line of sight. The applied corrections never exceed a few centimetres
333 over time scales of several hours, corresponding to path delay rates of $\approx 2 \times 10^{-6}$ m/s.
334 Although inherently small, these effects can be further reduced thanks to GPS-based
335 calibrations.

336 According to models of Doppler noise in Ka-band interplanetary radio links¹², solar
337 wind turbulence becomes a dominant noise source only at solar elongation angles lower
338 than 15° when partial calibration aided by the X-band radio link is available^{11,24}. For
339 Juno the expected interplanetary plasma noise in PJ3 (elongation = 61.6°) and PJ6
340 (elongation = 135.4°) is respectively 3×10^{-7} m/s and 1×10^{-7} m/s at 60 s integration times.
341 These values are well below the contributions expected from wet troposphere and
342 antenna mechanical noise¹². Path delay variations due to tropospheric water vapour
343 were calibrated using two microwave radiometers located near the ground antenna, with
344 parallel lines of sight. After calibrations, Doppler residuals integrated over 60 s were
345 reduced by about 30%.

346 The relevant time scale of gravity measurements is determined by the spatial scale of
347 the gravity field and by the spacecraft velocity. For the gravity harmonic of degree l , the
348 time scale is roughly $\pi R_J / l V_{sc}$, where R_J is Jupiter's equatorial radius and V_{sc} is the
349 spacecraft velocity near pericenter. For $l=12$, the time scale of the gravity signal is about
350 300 s. Doppler measurements were integrated over 60 s prior to processing in order to
351 enable adequate sampling of the gravity signal. At this time scale the measured range
352 rate noise at Ka band was 2×10^{-5} m/s at 60 s, in line with the expectations from Ka band

353 radio link noise models¹². The PJ3 and PJ6 Doppler residuals after plasma and
 354 tropospheric calibrations, and the corresponding Allan deviations are shown in
 355 Extended Data Fig. 1 and 2. The slope of the Allan deviation (approximately
 356 proportional to the inverse square root of the integration time) is consistent with a white
 357 Doppler noise between 4×10^{-4} and 2×10^{-2} Hz (the band of the gravity signal). The low
 358 Doppler noise experienced by Juno is much smaller than the gravity signal from the odd
 359 harmonics (example in Extended Data Fig. 3), facilitating their identification.

360 **Effect of the Io plasma torus.** Juno's radio signal invariably crosses the region of
 361 charged particles generated by the ionization of the gases emitted by Io's volcanos,
 362 known as the Io torus. The resulting path delay variation is a potentially important
 363 source of bias in the gravity estimates. The plasma density of the Io torus shows a
 364 variability of a factor of 2 over time scales of 20 days and is difficult to model²⁵. The
 365 path delay variation during a Juno pass can be estimated and partially calibrated by
 366 means of differential Doppler measurements in the X and Ka band. In PJ3 and PJ6 we
 367 measured path delay variations ascribed to the Io torus of about 2-4 cm at Ka band over
 368 a time scale of about two hours (16 times larger at X band).

369 The fractional frequency shift y of the received signal can be modelled as the sum of a
 370 non-dispersive contribution y_{ND} (dominated by the orbital dynamics) and a dispersive
 371 contribution due to charged particles:

$$y = y_{ND} + k \left(\frac{\dot{P}_U}{f_U^2} + \frac{\dot{P}_D}{\alpha^2 f_U^2} + \frac{\dot{I}_U}{f_U^2} + \frac{\dot{I}_D}{\alpha^2 f_U^2} \right) \quad (1)$$

372 Here f_U is the frequency of the signal transmitted by the ground station, α is the
 373 transponding ratio (the ratio between the frequency transmitted and received by the
 374 spacecraft), \dot{P}_U , \dot{P}_D , \dot{I}_U , and \dot{I}_D are the time derivatives of the columnar electron content
 375 (TEC) from the interplanetary and ionospheric plasma (P), and Io torus (I), respectively
 376 in the uplink (U) and downlink (D) path. The constant $k = e^2 / (8\pi^2 \epsilon_0 m_e c)$ is

377 approximately 1.34×10^{-7} m²/s. When multiple frequencies are available, the dispersive
 378 terms can be fully or partially measured thanks to the frequency dependence of the
 379 plasma refractive index^{11,24}.

380 Due to the difference in the X and Ka band transponding ratios (respectively 880/749
 381 and 3360/3599), in PJ3 and PJ6 the overall plasma contribution can be estimated to a
 382 75% accuracy¹¹. Under the assumption $\dot{I}_U = \dot{I}_D$ (well verified because the Io torus is just
 383 within 1.5 light-seconds from Juno), the frequency shift due to the Io torus is obtained
 384 by differencing the X and Ka band relative frequency shift described by Eq. 1:

$$\begin{aligned}
 & k \left(\frac{1}{f_K^2} + \frac{1}{\alpha_K^2 f_K^2} \right) \dot{I} \\
 &= \left(\frac{f_K^2 \alpha_K^2 \alpha_X^2 + 1}{f_X^2 \alpha_X^2 \alpha_K^2 + 1} - 1 \right)^{-1} \left\{ y_X - y_K \right. \\
 & \quad \left. - k \left[\dot{P}_U \left(\frac{1}{f_X^2} - \frac{1}{f_K^2} \right) + \dot{P}_D \left(\frac{1}{\alpha_X^2 f_X^2} - \frac{1}{\alpha_K^2 f_K^2} \right) \right] \right\}
 \end{aligned} \tag{2}$$

385 In Eq. 2, the estimated Io torus signal is contaminated by the uplink and downlink
 386 interplanetary plasma TEC variations. In PJ3 and PJ6 data we observed a residual
 387 plasma noise of about 8×10^{-7} m/s (relative frequency shift 2.7×10^{-15}) at 60 s integration
 388 time. We have assessed the effect of this error by means of numerical simulations.

389 Simulated Doppler observables of PJ3 and PJ6 were generated using the same
 390 dynamical model adopted in the analysis of PJ3 and PJ6 data. A white Gaussian noise
 391 with a standard deviation equal to the observed one was added to the simulated
 392 observables. Then, we have added a signal mimicking the effect of the Io torus to the
 393 simulated Doppler observables using a simple Gaussian model for the path delay Δl on
 394 a signal of frequency f :

$$\Delta l = \Delta l_K \left(\frac{f_K}{f} \right)^2 \exp \left[-\frac{1}{2} \left(\frac{t - \Delta \tau}{\tau/6} \right)^2 \right] \tag{3}$$

395 Here Δl_K is the maximum path delay on a signal with frequency f_K , τ is the total duration
 396 of the torus signal (corresponding to 6 standard deviation of a Gaussian curve), and $\Delta\tau$
 397 is the delay between the time of maximum path delay and the orbit pericenter. The
 398 values of the parameters adopted for each flyby were derived from direct measurements
 399 carried out in PJ3 and PJ6. $\Delta l_K = (2.1; 4.6)$ cm, $\tau = (120; 150)$ min, $\Delta\tau =$
 400 $(-15; +10)$ min provide a good match to PJ3 and PJ6 observations, respectively. The
 401 fractional frequency shift Δy on the Doppler observables is given by:

$$\Delta y = \frac{\dot{\Delta}l}{c} = - \left(\frac{f_X}{f} \right)^2 \frac{\Delta l_K}{c} \frac{t - \Delta\tau}{\tau/6} \exp \left[- \frac{1}{2} \left(\frac{t - \Delta\tau}{\tau/6} \right)^2 \right] \quad (.4)$$

402 To simulate the calibration error due to the residual plasma noise in Eq. 2, the
 403 calibrations were generated using the same model, but perturbing the input parameters
 404 with white, Gaussian random values. The standard deviations of the perturbing terms
 405 were chosen in order to match the observed solar plasma noise. The resulting standard
 406 deviation of the path delay δ is less than 10% of its value.

407 We then carried out a Monte Carlo simulation using 1000 noise realisations and
 408 obtained a sample of estimated gravity fields. None of the gravity harmonic coefficients
 409 changes by more than 1σ (see Extended Data Fig. 4 and 5 for examples). On the
 410 contrary, the Io torus can cause biases up to about 5σ on gravity solutions based on X
 411 band data. The most affected gravity coefficients are J_2 , J_3 , and J_4 .

412 **Tesseral gravity field.** The solution reported in Table 1 includes only degree 2 tesseral
413 gravity harmonics. Although higher degree tesseral harmonics are not required to fit the
414 data to the noise level, a higher degree field is certainly present. In order to assess the
415 effect of a tesseral field on the actual estimate, simulations with synthetic Doppler data
416 have been conducted. Thermal winds models with a scale height of 1900 km, consistent
417 with the observed odd harmonics³ but with a different scale height for the vortices
418 (associated to the tesseral component) have been used to generate synthetic gravity
419 fields. The resulting simulated Doppler observables have been fitted with the dynamical
420 model used to obtain our solution (Table 1), limited to degree 2 tesseral harmonics. Our
421 goal is to identify the largest tesseral field (therefore the largest scale height) that can be
422 hidden in the Doppler data without producing signatures in the residuals. We found that
423 the threshold value of the scale height is about 380 km.

424 To include the effect of the neglected tesseral field in the estimation, a consider analysis
425 has been performed. The consider analysis quantifies the effect of non-estimated
426 parameters (the higher degree tesseral field) on the uncertainties of the estimated
427 parameters. The effect on the estimate is an increase in the uncertainties. Extended Data
428 Table 2 reports the consider uncertainties of the estimate for a thermal wind model
429 having a scale height of the vortices of 380 km.

430 **Data availability**

431 The Juno tracking data and the ancillary information used in this analysis are archived at
432 NASA's Planetary Data System (<https://pds.nasa.gov>).

433

434 **Code availability**

435 The analysis presented in this work relies on proprietary orbit determination codes that
436 are not publicly available. The MONTE software package is used at the Jet Propulsion
437 Laboratory for planetary spacecraft navigation. The ORACLE orbit determination filter
438 was developed at Sapienza University of Rome under contract with the Italian Space
439 Agency.

440

441 **References**

- 442 23. Available at the web page <https://ssd.jpl.nasa.gov>
- 443 24. Mariotti, G. & Tortora, P. Experimental validation of a dual uplink
444 multifrequency dispersive noise calibration scheme for deep space tracking,
445 *Radio Sci.*, **48**, 1-7 (2013).
- 446 25. Delamere, P. A. & Bagenal, F. Modeling variability of plasma conditions in the
447 Io torus. *J. Geophys. Research: Space Phys.* **108**, A7 (2003).
448

449 **Extended data legends**

450 **Table ED1.** Characteristics of perijove passes PJ3 and PJ6 used in the gravity solution.

451 Altitude refers to the oblate planet. NON (negative orbit normal) to Earth is the angle
452 between the opposite of the orbit normal and the Earth direction. Longitude at equator
453 crossing refers to System III.

454 **Table ED2.** Consider covariances (3σ) when a tesseral field corresponding to a flow
455 depth of 380 km is added to the estimated zonal field in Table 1. Gravity fields
456 generated by larger depths of the tesseral flow would produce signatures in the Doppler
457 residuals²¹.

458 **Figure ED1. Range rate residuals.** Two-way range rate residuals (integrated over 60 s)
459 for the Ka-band pericenter passes PJ3 and PJ6. The rms value is 0.015 mm/s for both
460 passes. The sky frequencies were obtained from the radio science open loop receiver.

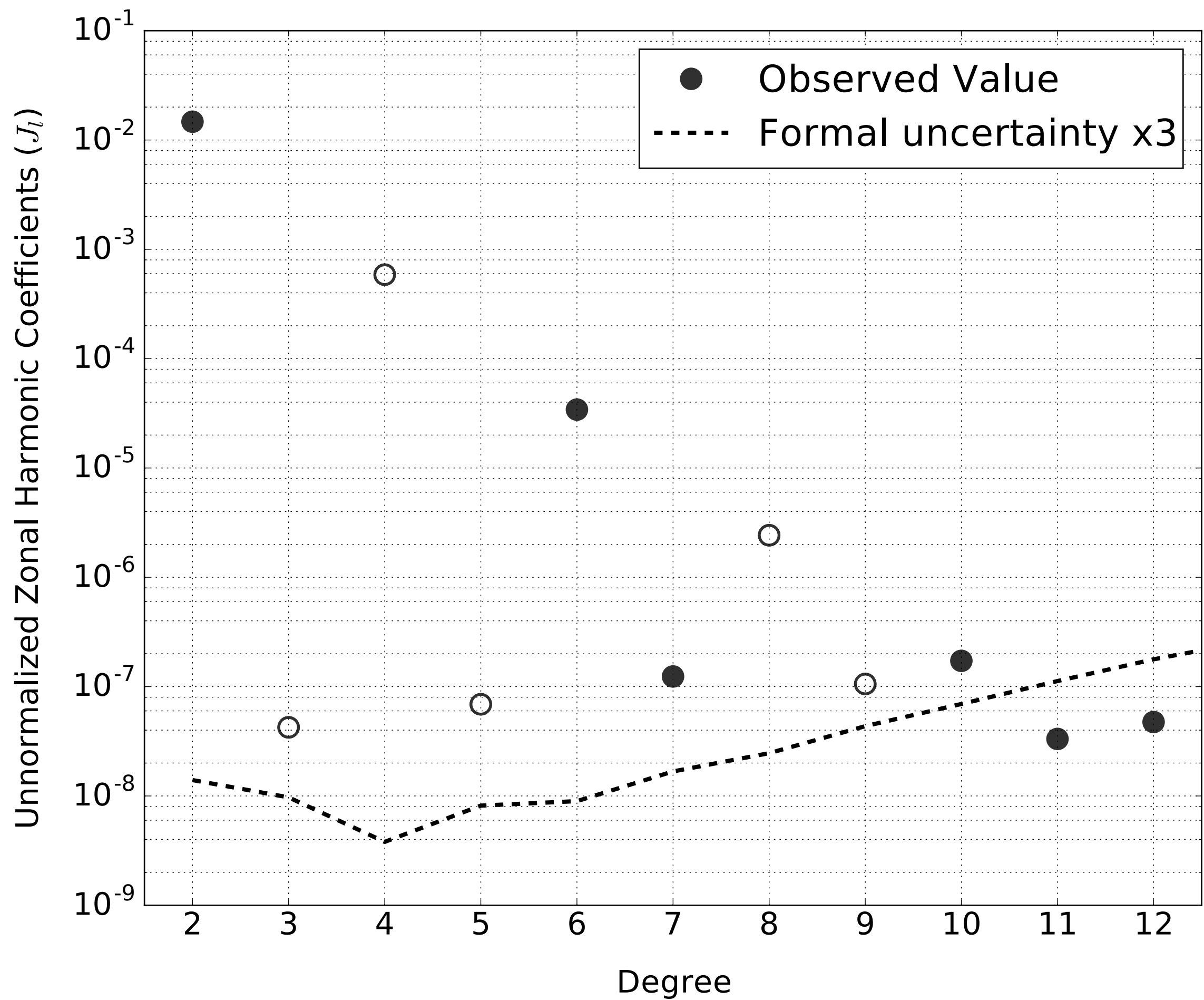
461 **Figure ED2. Frequency stability.** Allan deviation of relative frequency shift for the
462 Ka-band pericenter passes PJ3 and PJ6. The slopes are roughly consistent with a white
463 frequency noise (dashed line).

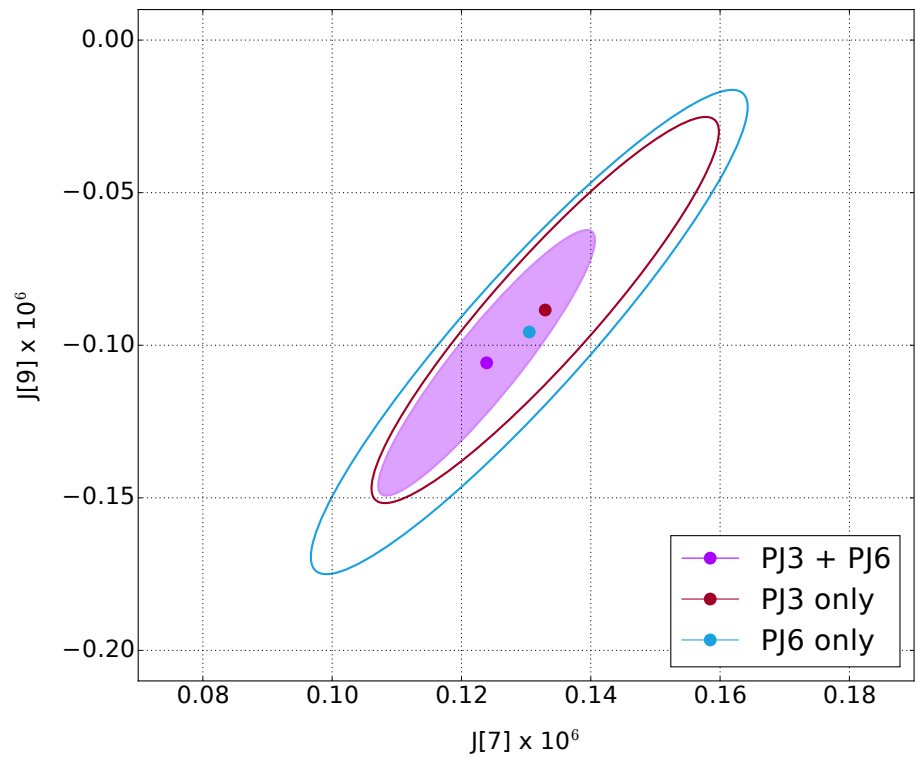
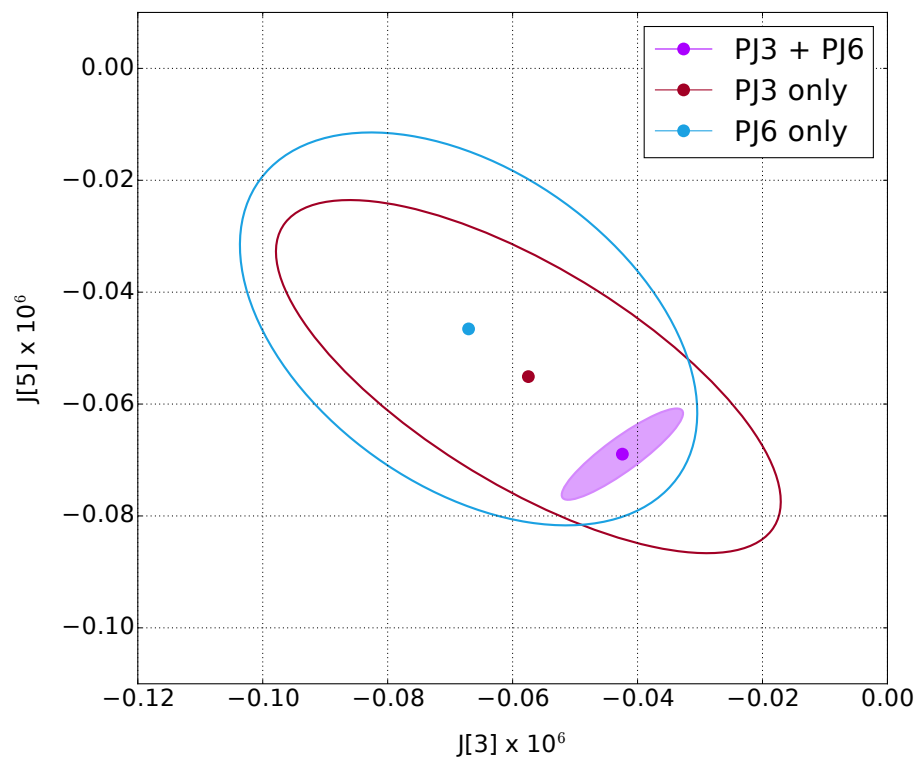
464 **Figure ED3. Gravity harmonic signatures.** Range rate signals from J_3 , J_5 , J_7 and J_9
465 gravity harmonics for PJ3 and PJ6. The smaller signal in PJ6 is due to a less favourable
466 projection of the spacecraft velocity along the Earth-Jupiter line of sight (the angle
467 between the Juno orbit normal and the line of sight was 19.2° in PJ3 and 15.1° in PJ6).
468 By comparison, the range rate noise at 60 s is 0.015 mm/s in both passes.

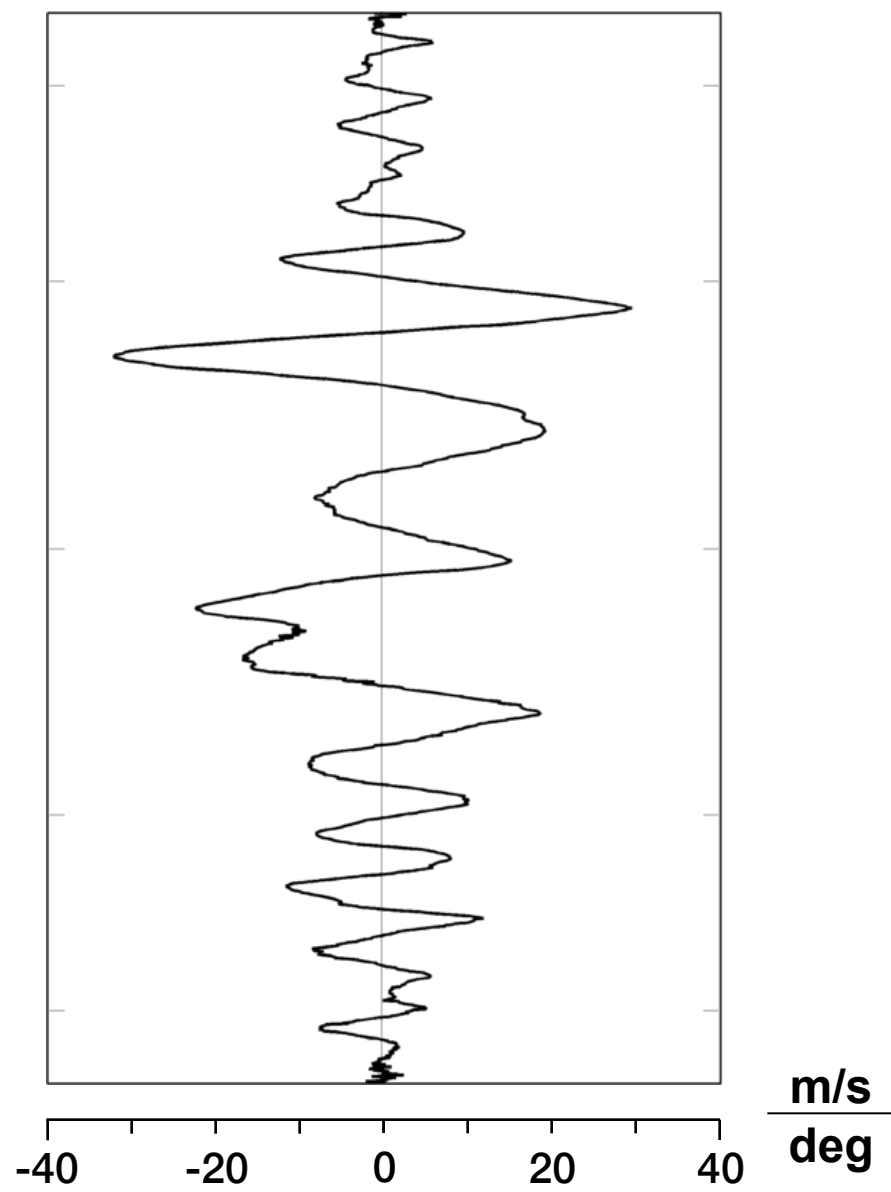
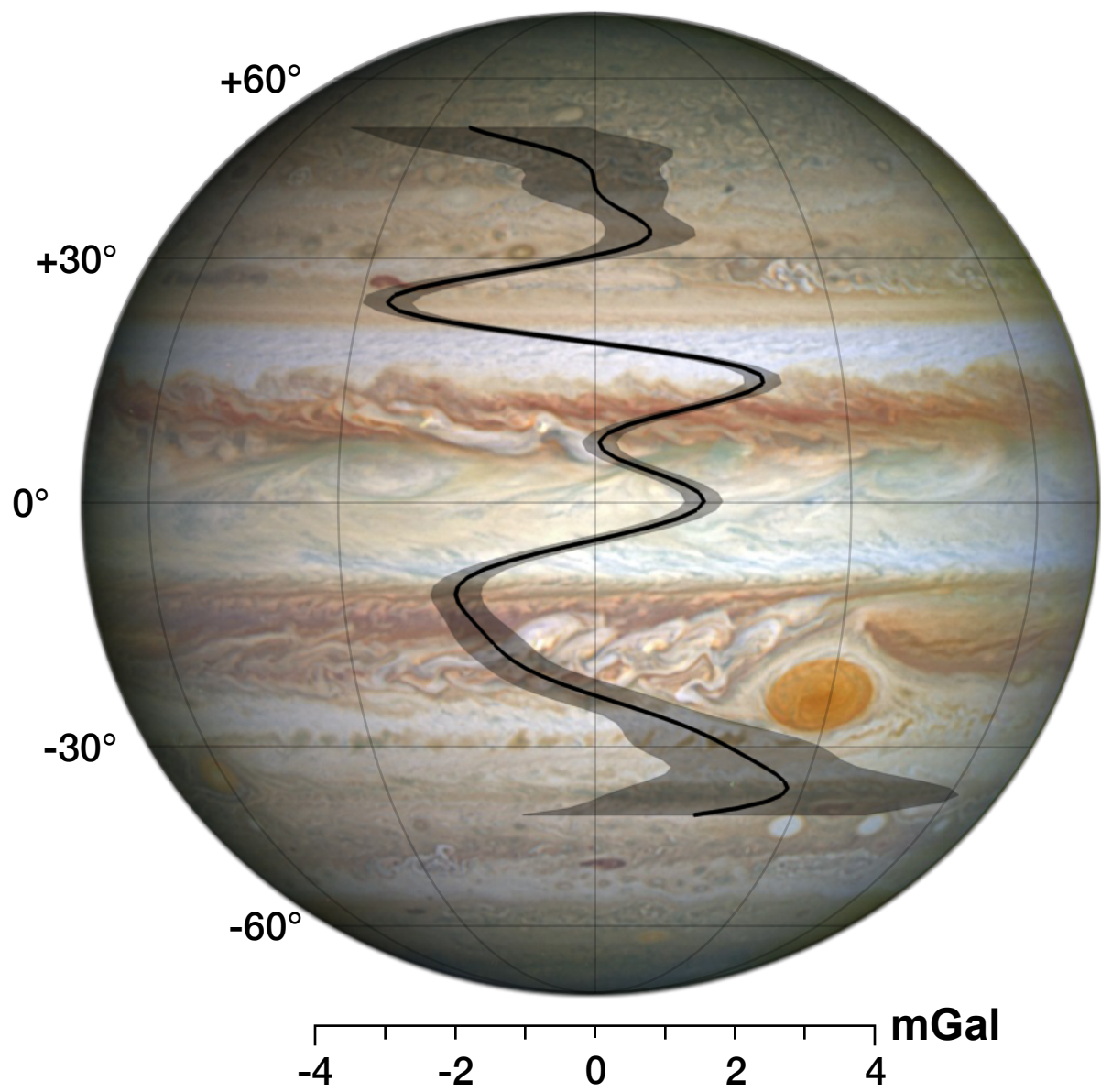
469 **Figure ED4. Io torus effects on J_3 - J_5 estimation.** Estimation biases on J_3 and J_5 due to
470 calibration errors of the Io torus path delay variation (cyan dots) in a Monte Carlo (MC)
471 simulation of the Juno PJ3-PJ6 gravity experiment. The calibration errors are compared
472 to the estimated 3σ uncertainty ellipses of the target solution (black), obtained without

473 the Io torus, and the solutions obtained using X- (red) and Ka-band data only (blue).
474 The estimation bias on J_3 is about 3σ if X-band data are used. Ka-band data or dual-link
475 calibration reduce the bias to less than 1σ .

476 **Figure ED5. Io torus effects on J_2 - J_4 estimation** Estimation biases on J_2 and J_4 from
477 the Monte Carlo simulation as in Fig. 1. The estimation bias on J_2 and J_4 is larger than
478 4σ if X-band data are used, while using Ka-band or plasma calibrated data it reduces to
479 less than 1σ .







	Value	Uncertainty
J_2 ($\times 10^6$)	14696.572	0.014
C_{21} ($\times 10^6$)	-0.013	0.015
S_{21} ($\times 10^6$)	-0.003	0.026
C_{22} ($\times 10^6$)	0.000	0.008
S_{22} ($\times 10^6$)	0.000	0.011
J_3 ($\times 10^6$)	-0.042	0.010
J_4 ($\times 10^6$)	-586.609	0.004
J_5 ($\times 10^6$)	-0.069	0.008
J_6 ($\times 10^6$)	34.198	0.009
J_7 ($\times 10^6$)	0.124	0.017
J_8 ($\times 10^6$)	-2.426	0.025
J_9 ($\times 10^6$)	-0.106	0.044
J_{10} ($\times 10^6$)	0.172	0.069
J_{11} ($\times 10^6$)	0.033	0.112
J_{12} ($\times 10^6$)	0.047	0.178
k_{22}	0.625	0.063
RA (deg)	268.0570	0.0013
Dec (deg)	64.4973	0.0014